Optical Stark effect in the four-wave mixing and stimulated Raman spectra of N₂

H. Moosmüller and C. Y. She Department of Physics, Colorado State University, Fort Collins, Colorado 80523

Winifred M. Huo

NASA Ames Research Center, Moffet Field, California 94035 (Received 25 May 1989; revised manuscript received 27 July 1989)

The influence of the optical Stark effect on spectral line shapes in four-wave-mixing Raman spectroscopy (FWMRS) and stimulated Raman spectroscopy (SRS) is investigated experimentally and theoretically. While both high-resolution spectroscopic techniques commonly use focused Gaussian beams with rather high laser intensities, the contribution of the optical Stark effect to the line shapes has not been well explored. Using an experimental setup, capable of rapid alternation between the simultaneous measurement of coherent Stokes Raman spectroscopy and inverse Raman spectroscopy spectra at low (mild-focusing) and high (tight-focusing) intensities, together with a sophisticated frequency reference scheme, we are able to perform a rather direct comparison between Stark-broadened and non-Stark-broadened spectra of both classes of Raman spectroscopies. Experimental spectra of lines in the vibrational Q branch of molecular nitrogen (N_2) are obtained for low and high pump-laser peak intensities in copropagating focused Gaussian beams. At high pump intensities, the optical Stark effect leads to strong asymmetric broadening for both types of coherent Raman spectroscopy. Our experimental results demonstrate that SRS spectra show more Stark shift and broadening than their FWMRS counterparts. Using the theory of signal generation in focused Gaussian beams, we have generated theoretical Stark-broadened spectra for both spectroscopies. While the experimental SRS spectra show excellent agreement with theoretical calculations, simultaneously measured FWMRS spectra do not perfectly agree with our theory. We demonstrate that this discrepancy can be partly reconciled by the inclusion of a resonant fifth-order process in the commonly employed third-order theory of FWMRS.

I. INTRODUCTION

The common use of high-power pulsed lasers in coherent Raman spectroscopies 1,2 (CRS) has led to increased interest in the influence of the optical Stark effect on vibrational and rotational transitions and the resulting changes in spectral line shapes. Previous investigations with both four-wave-mixing Raman spectroscopy [FWMRS,³ i.e., coherent Stokes Raman spectroscopy (CSRS) or coherent anti-Stokes Raman spectroscopy (CARS)] and stimulate Raman spectroscopy [SRS,² i.e., stimulated Raman gain spectroscopy (SRGS) or inverse Raman spectroscopy (IRS)] have largely been limited to spatially constant Stark-inducing fields.4,5 While this is the appropriate method to measure Stark coefficients, little has become known about the influence of the optical Stark effect on spectral line shapes taken with typical experimental setups. One exception is an investigation of ac-Stark-broadened line shapes in two-photon resonant multiphoton ionization,⁶ which closely resemble those in SRS. Most experimental setups use focused laser beams with more or less Gaussian profiles, this makes it necessary to investigate the interplay between optical Stark effect and signal generation in focused Gaussian beams, theoretically and experimentally for different CRS's. The large intensity variation in Gaussian beams leads to a distribution of Stark shifts within the beam, which has to be connected with the distribution of the signal generation in the respective Raman spectroscopy. The Stark effect itself destroys the degeneracy of the orientational (magnetic) sublevels of each rotational state. Therefore we have to calculate the Stark shift and the fractional transition strength for each sublevel. We have done this for rovibrational Raman transitions in molecular nitrogen (N_2). Nitrogen is an important example of a homonuclear diatomic molecule, whose rovibrational transitions can not be investigated with the usual methods of infrared spectroscopy. Furthermore, CRS in nitrogen has found many applications in combustion and flow diagnostics. $^{8-10}$

Section II derives Stark coefficients and fractional transition strengths for various Raman transitions in a diatomic homonuclear molecule in the $^1\Sigma^+$ state. Actual values of transition probabilities, for the example of N_2 , are evaluated by ab initio calculation. In Sec. III we give a short description of the experimental setup. Section IV presents experimental results, including simultaneously measured CSRS and IRS spectra of both Stark-broadened and non-Stark-broadened lines in the $v=0 \rightarrow v=1$ Q-branch vibrational spectrum of molecular nitrogen. These spectra are compared with theoretical calculations based on the theory of signal generation in focused Gaussian beams, 7 and theoretically evaluated fractional transition and Stark coefficients. The inclusion of a resonant fifth-order contribution in the third-order theory of

four-wave-mixing processes is discussed in Sec. V. Section VI gives a brief conclusion of this study.

II. THEORY

Under the influence of a strong electrical field, the degeneracy of the 2l+1 orientational (magnetic) sublevels (quantum number $m = -l, -l+1, \ldots, l-1, l$) of a molecular rotational energy level, characterized by the quantum number l, is lifted, with the exception of the ±m two-fold degeneracy. A ro-vibrational Raman transition labeled as $v, l \rightarrow v', l'$ in a weak field is split into the multitude of $v, l, |m| \rightarrow v', l', |m'|$ transitions in a strong electrical field. For each of these transitions, one has to know its individual Stark coefficient $\beta_{v',l',m'}^{v,l,m}$ and fractional transition strength $F_{v',l',m'}^{v,l,m}$, in order to predict experimental line shapes under strong fields.

A. Fractional transition strength

In coherent Raman spectroscopy the signal is related to the third-order nonlinear susceptibility $\chi_{ijkl}^{(3)}$. Using a damped-harmonic-oscillator model driven by the beating of two laser frequencies, ω_1 and ω_2 , this fourth-rank tensor may be expressed as $^{10-12}$

$$\chi_{ijkl}^{(3)}(\omega) = \frac{N\epsilon_0}{8\Delta} [(\Delta - \omega) - i\gamma]^{-1} \alpha'_{ij} \alpha'_{kl} , \qquad (1)$$

where Δ is the molecular transition frequency, $\omega = |\omega_2 - \omega_1|$, N the number of molecules per unit volume, and 2γ the damping constant. Here, α' stands for $(\partial \alpha/\partial q)_0$, the derivative of the molecular polarizabili-

$$\langle v', l', m' | \alpha | v, l, m \rangle = \langle v', l', m' | \alpha | v, l, m \rangle \delta_{v, v'} + \left[\frac{h}{4\pi\Delta} \right]^{0.5} [(v+1)^{0.5} \delta_{v', v+1} + (v)^{0.5} \delta_{v', v-1}] \langle v', l', m' | \alpha' | v, l, m \rangle.$$
(3b)

The first term $\langle v', l', m' | \alpha | v, l, m \rangle \delta_{v,v'}$ is responsible for Rayleigh and rotational Raman scattering, while the other two terms result in Stokes and anti-Stokes vibrationalrotational Raman scattering. For transitions between v=0 and v'=1, which are of interest to this paper, Eq. (2) may be rewritten as

$$\chi_{ijkl}^{(3)} = \sum_{l,m} \sum_{l',m'} \widetilde{A}_{1,l',m'}^{0,l,m} \langle l',m' | \alpha_{ij} | l,m, \rangle^*$$

$$\times \langle l',m' | \alpha_{kl} | l,m \rangle . \tag{4}$$

where $\widetilde{A}_{1,l',m'}^{0,l,m} = (\pi\epsilon_0/2h)N[(\Delta_{1,l',m'}^{0,l,m} - \omega) - i\gamma]^{-1}$, and α stands here and in the following for $\alpha_{v'}^v = \langle v' | \alpha | v \rangle$ with v'=1 and v=0. We have changed from $\alpha'=(\partial \alpha/\partial q)_0$ in Eq. (2) to α_1^0 , because the latter will be evaluated by ab initio calculation without the simple-harmonicoscillator approximation.

To simplify the respective transition-matrix elements, in a way that their rotational-orientational parts may be evaluated directly, we introduce a laboratory coordinate system with unit vectors $\hat{\mathbf{x}}$, $\hat{\mathbf{y}}$, and $\hat{\mathbf{z}}$, and a coordinate system for an individual molecule with unit vectors $\hat{\mathbf{X}}$, $\hat{\mathbf{Y}}$ and $\hat{\mathbf{Z}}$ as shown in Fig. 1. For a diatomic molecule such as N_2 , we choose \hat{Z} parallel to the internuclear axis and designate α_Z as α_{\parallel} . Due to the symmetry of diatomic

ty tensor with respect to the generalized vibrational coordinate q of the harmonic oscillator. Equation (1) can be derived either classically^{10,11} or quantum mechanically.¹² In a real molecule, such as N₂, all allowed transitions, each with a transition frequency $\Delta_{v',l',m'}^{v,l,m}$ and an assumed identical damping constant 2γ , must be accounted for and summed over. The third-order tensor $\chi_{ijkl}^{(3)}$ then be-

$$\chi_{ijkl}^{(3)} = \sum_{v,l,m} \sum_{v',l',m} A_{v',l',m'}^{v,l,m} \langle v',l',m'|\alpha'_{ij}|v,l,m \rangle^*$$

$$\times \langle v',l',m'|\alpha'_{kl}|v,l,m \rangle , \qquad (2)$$

with

$$A_{v',l',m'}^{v,l,m} = \frac{N\epsilon_0}{8\Delta_{v',l',m'}^{v,l,m}} [(\Delta_{v',l',m'}^{v,l,m} - \omega) - i\gamma]^{-1} .$$

Under the assumption of a small vibrational amplitude, the vibrational transition-matrix element of the electronic polarizability α may be expanded as

$$\langle v', l', m' | \alpha | v, l, m \rangle = \langle v', l', m' | (\alpha)_0 | v, l, m \rangle + \langle v' | q | v \rangle \times \left\langle v', l', m' \left| \left(\frac{\partial \alpha}{\partial q} \right)_0 \right| v, l, m \right\rangle.$$
(3a)

Substituting the reduced matrix elements $\langle v'|q|v \rangle$ of the simple harmonic oscillator with unity mass, 13 we have

$$\frac{1}{\Delta} \int_{0.5}^{0.5} [(v+1)^{0.5} \delta_{v',v+1} + (v)^{0.5} \delta_{v',v-1}] \langle v',l',m' | \alpha' | v,l,m \rangle .$$
(3b)

molecules, the polarizability α is degenerate in the \hat{X} - \hat{Y} plane and we designate $\alpha_X = \alpha_Y$ as α_1 . In the molecular coordinate system these are the only nonzero elements of the polarizability tensor. Coordinate transformation yields the following polarizability tensor in the laboratory coordinate system:

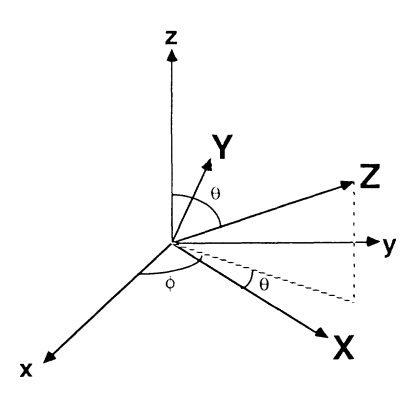


FIG. 1. Laboratory (x,y,z) and molecular (X,Y,Z) coordinate systems appropriate for a diatomic molecule, with the molecular Y axis chosen to be in the x-y plane.

$$\alpha = \begin{bmatrix} (\alpha_{\parallel} - \alpha_{\perp}) \sin^2\theta \cos^2\phi + \alpha_{\perp} & (\alpha_{\parallel} - \alpha_{\perp}) \sin^2\theta \sin\phi \cos\phi & (\alpha_{\parallel} - \alpha_{\perp}) \sin\theta \cos\theta \cos\phi \\ (\alpha_{\parallel} - \alpha_{\perp}) \sin^2\theta \sin\phi \cos\phi & (\alpha_{\parallel} - \alpha_{\perp}) \sin^2\theta \sin^2\phi + \alpha_{\perp} & (\alpha_{\parallel} - \alpha_{\perp}) \sin\theta \cos\theta \sin\phi \\ (\alpha_{\parallel} - \alpha_{\perp}) \sin\theta \cos\theta \cos\phi & (\alpha_{\parallel} - \alpha_{\perp}) \sin\theta \cos\theta \sin\phi & (\alpha_{\parallel} - \alpha_{\perp}) \cos^2\theta + \alpha_{\perp} \end{bmatrix}.$$

$$\begin{pmatrix}
(\alpha_{\parallel} - \alpha_{\perp})\sin\theta\cos\theta\sin\phi \\
(\alpha_{\parallel} - \alpha_{\perp})\cos^{2}\theta + \alpha_{\perp}
\end{pmatrix} .$$
(5)

Due to the symmetry properties of $\chi^{(3)}$, we need not calculate the transition matrix elements for all components of the polarizability, but may restrict the calculations to α_{13} , α_{23} , and α_{33} . Using the explicit expressions for the spherical harmonics Y_l^m we write l3,14

$$\alpha_{13} = (2\pi/15)^{0.5} \gamma_{v'}^{v} (Y_2^{-1} - Y_2^1)$$
, (6a)

$$\alpha_{23} = i(2\pi/15)^{0.5} \gamma_{\nu}^{\nu} (Y_2^{-1} + Y_2^{1}),$$
 (6b)

$$\alpha_{33} = a_{v'}^{v} + \frac{4}{3}(\pi/5)^{0.5} \gamma_{v'}^{v} Y_2^0$$
, (6c)

where the invariants of the polarizability tensor a and γ are defined as $a=(\alpha_{\parallel}+2\alpha_{\perp})/3$ and $\gamma=\alpha_{\parallel}-\alpha_{\perp}$ and the matrix elements $\langle l',m'|\alpha_{ij}|l,m\rangle$ may be evaluated in terms of Clebsch-Gordan coefficients. 11,15

In order to express $\chi^{(3)}$ in a more manageable form, we rewrite Eq. (4) as

$$\chi_{ijkl}^{(3)} = \sum_{l,m} \sum_{l',m'} \widetilde{A}_{1,l',m'}^{0,l,m} F_{l',m'}^{l,m} \times \left\{ \sum_{m} \sum_{m'} \langle l', m' | \alpha_{ij} | l, m \rangle^* \times \langle l', m' | \alpha_{kl} | l, m \rangle \right\}, \quad (7a)$$

with the fractional transition strength $F_{l',m'}^{l,m}$ defined as

$$F_{l',m'}^{l,m} = \frac{\langle l',m'|\alpha_{ij}|l,m\rangle^*\langle l',m'|\alpha_{kl}|l,m\rangle}{\sum_{m}\sum_{m'}\langle l',m'|\alpha_{ij}|l,m\rangle^*\langle l',m'|\alpha_{kl}|l,m\rangle}, \quad (7b)$$

and $\sum_{m} \sum_{m'} F_{l',m'}^{l,m} = 1$, by definition. Note that the quantity in the brackets of Eq. (7a) is independent of m and

m'; it depends only on the reduced matrix element α (or a and γ), l, and l'. In the case where Stark effect is negligible, \widetilde{A} becomes independent of m and m', yielding the common expression for $\chi^{(3)}$ in small fields. The remaining summation over l and l' takes care of the influence of neighboring lines. In terms of the matrix elements of a and a we can calculate two independent elements of a explicitly as

$$\chi_{3333}^{(3)} = \sum_{l,m} \sum_{l',m'} \tilde{A}_{l',m'}^{l,m} F_{l',m'}^{l,m} (a^2 + \frac{4}{45} b_{l'}^l \gamma^2) , \qquad (8a)$$

$$\chi_{2323}^{(3)} = \sum_{l,m} \sum_{l',m'} \widetilde{A}_{l',m'}^{l,m} F_{l',m'}^{l,m} \frac{1}{15} b_{l'}^{l} \gamma^{2} , \qquad (8b)$$

where a and γ strictly speaking stand for a_1^0 and γ_1^0 , respectively, and the well-known Placzek-Teller coefficients $b_{l'}^l$ are given as

$$b_{l-2}^{l} = \frac{3}{2} \frac{l(l-1)}{(2l+1)(2l-1)}$$
 (9a)

for the O branch,

$$b_l^l = \frac{l(l+1)}{(2l-1)(2l+3)} \tag{9b}$$

for the Q branch, and

$$b_{l+2}^{l} = \frac{3}{2} \frac{(l+1)(l+2)}{(2l+1)(2l+3)}$$
(9c)

for the S branch. These coefficients are a special case of the more general results for symmetric top molecules. ¹⁶ To obtain the rest of the 81 elements of $\chi^{(3)}$, we first use the fact that our polarizability α is a symmetric tensor, and write

TABLE I. Isotropic and anisotropic polarizabilities of N_2 , in units of $\mathring{A}^3 = 10^{-30} \text{ m}^3$.

TABLE 1. Isotropic and amsotropic polarizationities of 142, in times of A 10 m.									
1	a_0^0	a_1^1	a_{1}^{0}	γ_0^0	γ_1^1	γ_1^0			
0	21.895 220	22.080 880	0.690 539	8.621 598	8.864717	0.753 928			
1	21.895 360	22.081 020	0.690 545	8.621 748	8.864 854	0.753 945			
2	21.895 630	22.081 300	0.690 563	8.622 046	8.865 132	0.753 980			
3	21.896 040	22.081 710	0.690 589	8.622 490	8.865 545	0.754 036			
4	21.896 580	22.082 250	0.690 625	8.623 084	8.866 098	0.754 109			
5	21.897 270	22.082 940	0.690 671	8.623 827	8.866 789	0.754 200			
6	21.898 090	22.083 770	0.690727	8.624718	8.867 620	0.754 310			
7	21.899 040	22.084 730	0.690 790	8.625 758	8.868 587	0.754 439			
8	21.900 130	22.085 830	0.690 856	8.626 946	8.869 696	0.754 580			
9	21.901 360	22.087 060	0.690 936	8.628 285	8.870 944	0.754 744			
10	21.902 730	22.088 440	0.691 025	8.629 773	8.872 333	0.754 925			
11	21.904 220	22.089 950	0.691 124	8.631 409	8.873 861	0.755 122			
12	21.905 860	22.091 610	0.691 230	8.633 194	8.875 531	0.755 338			
13	21.907 640	22.093 400	0.691 345	8.635 131	8.877 344	0.755 573			
14	21.909 550	22.095 330	0.691 470	8.637 215	8.879 299	0.755 822			

$$\chi_{ijkl}^{(3)} = \chi_{ijlk}^{(3)} = \chi_{jikl}^{(3)} = \chi_{jilk}^{(3)} . \tag{10}$$

General symmetry considerations for isotropic media along with Eq. (10) make all 21 nonzero elements expressible 17 in terms of two independent elements $\chi_{3333}^{(3)}$ and $\chi_{3323}^{(3)}$. To evaluate the fractional transition strength $F_{l,m}^{l,m}$, we limit the calculation to our experimental situation, where the polarizations of pump and probe laser and detection system are all parallel, i.e., i=j=k=l. In

this case we have $\Delta m = 0$, and the fractional transition strengths for the degenerate levels +m and -m are identical $(F_l^{l,m} = F_l^{l,-m})$. In this case the explicit evaluation of Eq. (7b) for the different Raman branches yields with i = j = k = l

$$F_{l-2,m}^{l,m} = \frac{15}{2} \frac{(l^2 - m^2)[(l-1)^2 - m^2]}{l(l-1)(2l-3)(4l^2 - 1)}$$
(11a)

for the O branch,

TABLE II. Stark coefficients $\beta_{1,l,m}^{0,l,m}$ (mm²J⁻¹) and relative transition strengths $F_{1,l,m}^{0,l,m}$ for some lines in the Q branch of N_2 .

l	m	$oldsymbol{eta}_{1,l,m}^{\scriptscriptstyle 0,l,m}$	$F_{1,l,m}^{0,l,m}$	l	m	$oldsymbol{eta}_{1,l,m}^{\scriptscriptstyle 0,l,m}$	$F_{1,l,m}^{0,l,m}$
0	0	-0.467 31	1.000 00	9	0	-0.57008	0.071 81
1	0	-0.63050	0.533 09	9	1	-0.56665	0.142 14
1	1	-0.38573	0.46691	9	2	-0.55639	0.137 74
2	0	-0.58386	0.283 26	9	3	-0.53928	0.130 57
2	1	-0.52559	0.473 19	9	4	-0.51533	0.120 84
2	2	-0.35077	0.243 55	9	5	-0.48453	0.108 89
}	0	-0.57609	0.198 10	9	6	-0.44689	0.095 13
3	1	-0.54890	0.364 66	9	7	-0.40241	0.080 07
}	2	-0.46733	0.277 86	9	8	-0.35109	0.064 30
3	3	-0.33138	0.159 38	9	9	-0.29292	0.048 5
Ļ	0	-0.57326	0.152 89	10	0	-0.56990	0.064 95
Į.	1	-0.55737	0.291 37	10	1	-0.56711	0.128 79
1	2	-0.50971	0.25022	10	2	-0.55872	0.125 54
ŀ	3	-0.43027	0.188 59	10	3	-0.54475	0.120 20
ŀ	4	-0.31906	0.11693	10	4	-0.52519	0.112 92
5	0	-0.57189	0.124 63	10	5	-0.500 05	0.103 90
5	1	-0.56144	0.241 48	10	6	-0.46931	0.093 38
5	2	-0.53007	0.218 88	10	7	-0.43298	0.0816
5	3	-0.47781	0.183 68	10	8	-0.39107	0.069 14
;	4	-0.40463	0.139 58	10	9	-0.34357	0.056 20
;	5	-0.31055	0.091 76	10	10	-0.29048	0.030 20
5	0	-0.57111	0.105 24	11	0	-0.56977	0.059 28
5	1	-0.56370	0.205 80	11	1	-0.56745	0.039 28
ó	2	-0.54146	0.192 09	11	2	-0.56047	0.117 /3
, 5	3	-0.50441	0.170 29	11	3	-0.54885	0.113 2.
ó	4	-0.45254	0.141 98	11	4	-0.53258	0.1111
, 5	5	-0.38584	0.109 35	11	5	-0.51165	0.103 5
, 5	6	-0.30432	0.109 33	11	6	-0.48608	
, 7	0	-0.57063	0.073 20	11	7		0.090 43
7	1	-0.565 09	0.091 09	11	8	-0.455 86	0.081 2
, 7	2				9	-0.420 99	0.071 18
7		-0.548 50	0.170 22	11		-0.38146	0.060 62
, 7	3 4	-0.52084	0.155 84	11	10	-0.33729	0.049 81
7		-0.48212	0.13678	11	11	-0.28847	0.039 11
,	5	-0.432 34	0.114 10	12	0	-0.56967	0.054 53
	6	-0.371 50	0.089 17	12	1	-0.56770	0.108 40
7	7	-0.299 59	0.063 66	12	2	-0.561 81	0.1064
3	0	-0.570 30	0.080 30	12	3	-0.551 99	0.103 29
3	1	-0.566 02	0.158 54	12	4	-0.53823	0.098 92
3	2	-0.55315	0.152 40	12	5	-0.52055	0.093 43
3	3	-0.53171	0.142 44	12	6	-0.498 94	0.086 94
3	4	-0.501 70	0.129 06	12	7	-0.47341	0.079 58
3	5	-0.463 11	0.112 83	12	8	-0.443 94	0.071 48
3	6	-0.415 94	0.094 47	12	9	-0.41054	0.062 83
}	7	-0.36020	0.074 87	12	10	-0.37322	0.053 82
3	8	-0.295 89	0.055 09	12	11	-0.33197	0.044 67
				12	12	-0.28678	0.035 63

$$F_{l,m}^{l,m} = \frac{1}{2l+1} \frac{\left[\alpha_{v'}^{v} - \frac{2}{3}\gamma_{v'}^{v} \frac{3m^{2} - l(l+1)}{(2l-1)(2l+3)}\right]^{2}}{(\alpha_{v'}^{v})^{2} + \frac{4}{45}(\gamma_{v'}^{v})^{2} \frac{l(l+1)}{(2l-1)(2l+3)}}$$
(11b)

for the Q branch,

$$F_{l+2,m}^{l,m} = \frac{15}{2} \frac{[(l+2)^2 - m^2)][(l+1)^2 - m^2]}{(l+1)(l+2)(2l+1)(2l+3)(2l+5)}$$
(11c)

for the S branch.

We have determined the isotropic and anisotropic polarizabilities a_0^0 , a_1^1 , a_1^0 , γ_0^0 , γ_1^1 , γ_1^0 , and the Raman transition matrix elements of N_2 based on the ab initio data of Langhoff et al., 18 who determined α_{\parallel} and α_1 as a function of internuclear distance. The vibrational wave functions used in the calculations of these matrix elements are numerical solutions of the one-dimensional Schrödinger equation with an RKR potential, 19 without using the simple-harmonic-oscillator approximation. The results are listed in Table I as a function of the rotational quantum number l. The ab initio results for both a_0^0 and γ_0^0 are in good agreement with experimental results. 20,21 The resulting numerical values of the fractional transition strength $F_{l',m}^{l'}$ for some lines in the Q branch of N_2 are listed in Table II.

B. Stark effect

The influence of strong electrical fields, either dc (static field) or at optical frequencies (laser field), on molecules leads to Stark effect, i.e., a shift of molecular energy levels as a function of the electric field. Homonuclear molecules do not have a permanent electrical dipole moment. The first-order Stark effect is zero and we are dealing with the second-order Stark effect. Therefore we must consider the magnitude of the induced dipole moment $p_0 = \epsilon_0 \alpha E_0$. The energy shift of the molecule in a dc electrical field is

$$W = -\epsilon_0 \alpha \int_0^{E_{\text{dc}}} E \ dE = -\frac{1}{2} \epsilon_0 \alpha E_{\text{dc}}^2 \ . \tag{12a}$$

For an optical electrical field we replace $E_{\rm dc}^2$ with the time average of the squared electrical field $\langle E^2 \rangle = \frac{1}{2} E_0^2$. Assuming the applied field is in the z direction, i.e., $\mathbf{E} = (0,0,E_3)$, we have

$$W = -\frac{1}{4}\epsilon_0 \alpha_{33} E_3^2 \ . \tag{12b}$$

Quantum mechanically we have to replace the tensor elements of α by the corresponding transition matrix element $\langle vlm | \alpha_{33} | vlm \rangle$, which can be calculated explicitly. Using the relationship between intensity I and electrical field amplitude E_0 , $I = \frac{1}{2}c\,\epsilon_0 E_0^2$, of an electromagnetic wave, we can write the resulting energy shift W due to the optical Stark effect as

$$W = \frac{-I}{2c} \left[a_v^v - \frac{2}{3} \gamma_v^v \frac{3m^2 - l(l+1)}{(2l-1)(2l+3)} \right]. \tag{13}$$

For a transition from a lower energy level v, l, m to a higher level v', l', m' the resulting shift of the transition

frequency is

$$\Delta v = \frac{1}{h} (W_{v',l',m'} - W_{v,l,m})$$

$$= \frac{-I}{2hc} \left[a_{v'}^{v'} - a_{v}^{v} - \frac{2}{3} \gamma_{v'}^{v'} \frac{3m'^{2} - l'(l'+1)}{(2l'-1)(2l'+3)} + \frac{2}{3} \gamma_{v}^{v} \frac{3m^{2} - l(l+1)}{(2l-1)(2l+3)} \right], \qquad (14)$$

where h is Planck's constant. For $\Delta m = 0$ transitions in the Q branch this equation simplifies to

$$\Delta v = \frac{-I}{2hc} \left[a_{v'}^{v'} - a_{v}^{v} - \frac{2}{3} (\gamma_{v'}^{v'} - \gamma_{v}^{v}) \frac{3m^{2} - l(l+1)}{(2l-1)(2l+3)} \right] . \quad (15)$$

Now we define the Stark coefficient β as

$$\beta_{v'l'm'}^{vlm} = \frac{\Delta v}{I} , \qquad (16)$$

and the resulting Stark coefficients β_{1lm}^{0lm} for nondepolarized ($\Delta m = 0$) Q-branch transitions in molecular nitrogen are listed in Table II. Under strong field, the intensity-dependent third-order susceptibility may be obtained from Eq. (4) or Eq. (7) with $\Delta_{v'l'm'}^{vlm}$ replaced by $\Delta_{v'l'm'}^{vlm} + \beta_{v'l'm'}^{vlm} I$.

III. EXPERIMENTAL SETUP

To perform CRS we use an experimental setup with two lasers (Fig. 2). A pulsed laser beam is generated by passing the output of a 70-mW single-mode tunable cw dye laser through a pulsed amplifier. This way we obtain 5-nsec pulses with a nearly Fourier-transform-limited linewidth of 116 MHz. The peak power is 2-4 MW at roughly 584.5 nm, and the repetition rate is 10 pulses/s. For the second (probe) laser we use a 514.5-nm cw single-mode Ar^+ -ion laser with roughly 200-mW output power and a line width of several megahertz. The fluorescence of a temperature-stabilized I_2 cell is used to lock the frequency of the Ar^+ -ion laser to the side of an I_2 line.

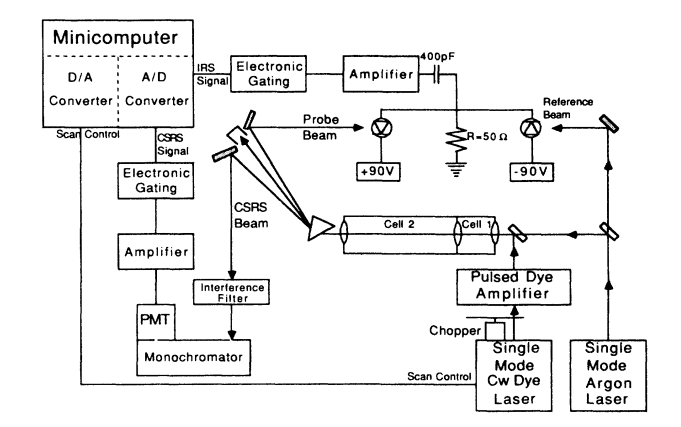


FIG. 2. Experimental setup.

Although for lasers with given power, SRGS and IRS signals are equally large in terms of photon numbers, the relative gain-loss depends on the power of the respective probe laser beam. With the pulsed dye laser being some seven orders of magnitude more powerful than the cw argon laser, the relative gain in SRGS is roughly seven orders of magnitude weaker than the relative loss in IRS. The situation for FWMRS is similarly asymmetric. While the CARS signal is proportional to $P_{\rm dye}P_{\rm argon}^2$, the CSRS signal is proportional to $P_{\rm dye}P_{\rm argon}^2$ and therefore some seven orders of magnitude stronger. Thus we chose to detect the IRS and CSRS signals.

The argon laser beam is divided by a beam splitter into probe and reference beams. A telescope is then used to match the argon laser beam size to that of the dye laser. We overlap dye and argon laser beams with a dichroic mirror and focus them with an air-spaced achromatic lens (f=5 cm) into the first cell. This focus is imaged into the second cell by another achromatic 5-cm lens. We position this lens so that the second focus occurs 50 cm behind it (Fig. 3). Therefore the second focus has ten times the spot size and 1% of the maximum intensity of the first focus. At the end of the second cell we use a simple 50-cm lends to collimate both beams. During the experiment, one of these cells is filled with nitrogen at a pressure of 10 kPa and a temperature of 292 K, while the other cell is evacuated. By evacuating one cell and filling the other, within less than a minute we can switch from CRS signals generated in a tight focusing arrangement (cell 1 filled, spectra with Stark effect) to signals generated in a mild focusing arrangement (cell 2 filled, spectra without Stark effect), without any realignment of optical components.

At the front end of the second gas cell we can insert a parallel glass plate to reflect part of the beam out of the cell. This way the beam can be profiled by the following arrangement (Fig. 3). A photodiode, mounted directly behind a 5- μ m slit is scanned with a motorized translation stage across the beam and beam profiles can be recorded. In the case of a cw beam the photodiode output is simply amplified and digitized, while for pulsed

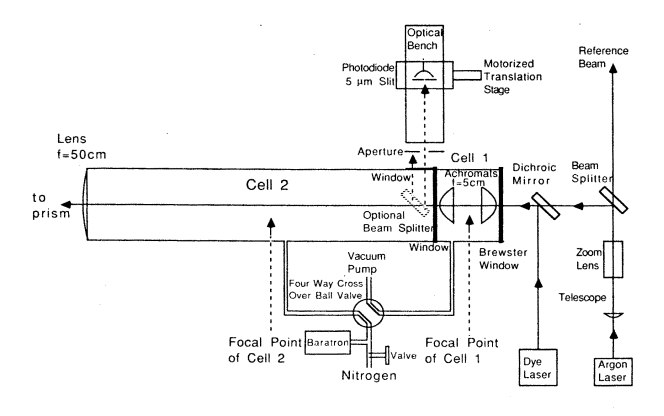


FIG. 3. Setup for coherent Raman spectroscopy with two gas cells.

beam, we use a gated integrator to sample the signal and store it between laser pulses for digitization. The translation stage is mounted on an optical bench parallel to the beam, so it can be easily moved to acquire beam profiles at different distances from the focal point. This way focal point, Rayleight length and spot size of both beams can be determined and matched. This procedure is rather time consuming, but once it has been completed, it does not have to be repeated until the basic setup is changed.

After passing through the cells, the beams are separated by a prism and the dye laser beam is blocked by a beam dump. The CSRS beam is spectrally filtered by a monochromator, colored glass, and interference filters to eliminate traces of pump laser light. A photomultiplier, mounted behind the monochromator detects the CSRS signal. The argon laser probe and reference beams are detected by fast photodiodes and we subtract the respective signals to eliminate argon laser intensity noise. Using the argon laser line at 514.5 nm, we tune the dye laser near 584.5 nm to be in resonance with the Q branch $v = 0 \rightarrow v = 1$ vibrational transition in molecular nitrogen (2330-cm⁻¹ Raman shift). We scan the dye laser digitially over the Raman resonances, with eight dye laser pulses per frequency step. IRS and CSRS signals are electronically gated and then simultaneously recorded on a shotto-shot basis by a minicomputer. To check for scan nonlinearities and measure the frequency of the dye laser, we split off a part of the cw dye beam before amplification and record, simultaneously with the Raman spectra, a saturated absorption spectrum of I2 and a transmission spectrum of a Fabry-Perto interferometer with a free spectral range of about 75 MHz.²³

IV. EXPERIMENTAL RESULTS AND COMPARISON WITH THE THEORY

Using the setup discussed in Sec. III, we have recorded spectra of several lines in the vibrational Q branch $(v=0 \rightarrow v \rightarrow 1)$ of molecular nitrogen (N_2) under various experimental conditions. Generally we alternate between recording spectra with and without Stark broadening. This makes it possible to separate the contributions of Stark broadening from other factors which contribute to Raman line shapes. To check our understanding of the contributions to the non-Stark broadened line shapes, we have analyzed spectra taken with low pump laser intensity. This analysis, which has found excellent agreement between theory and our experimental results, has been the subject of a recent publication.³ In this section, we first discuss our frequency linearization and frequency reference procedures, before we compare experimental spectra without and with the influence of optical Stark effect with respective theories.

Typical simultaneously recorded IRS, CSRS, iodine (I_2) , and Fabry-Perot (FP) spectra are shown in Figs. 4(a)-4(d), respectively. Each spectrum consists of 2^{10} (i.e., 1024) data points, each averaged over eight laser pulses at a constant dye laser frequency. The common x axis is a frequency scale derived from the analog voltage, which controls the dye laser scan, assuming a linear relationship between this voltage and the dye laser frequency. Due to the existence of unpredictable nonlinearities in

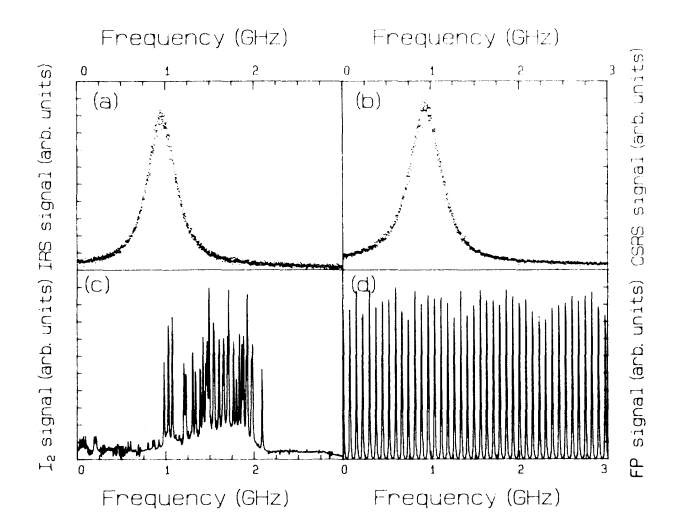


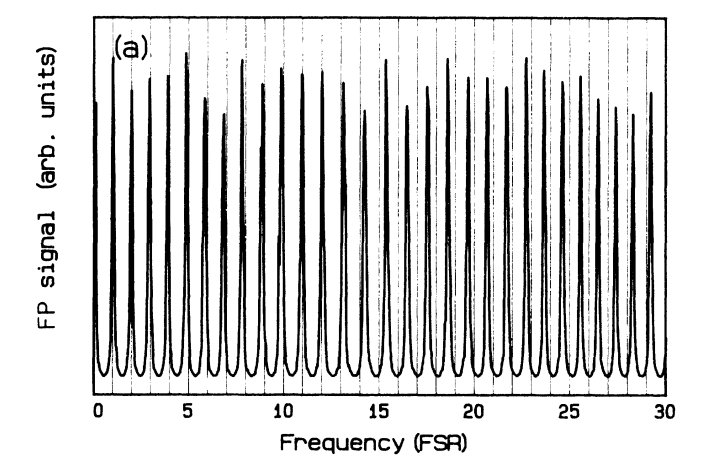
FIG. 4. Simultaneously recorded data. (a) IRS spectrum of the l=4 vibrational Q-branch transition $(v=0\rightarrow v=1)$ in molecular nitrogen. (b) CSRS spectrum of the l=4 vibrational Q-branch transition $(v=0\rightarrow v=1)$ in molecular nitrogen. (c) Doppler free spectrum of molecular iodine. (d) Transmission spectrum of the 75-MHz Fabry-Perot interferometer.

the laser scan mechanism, the relationship between this voltage and the actual laser frequency is neither exact nor reproducible. The irreproducible nonlinearities of our system are in the order of several percent. This nonlinearity is clearly seen in Fig. 5(a), where we plot a portion of the Fabry-Perot transmission spectrum previously shown in Fig. 4(d) against the frequency derived from the analog voltage, with a grid spacing corresponding to the free spectral range (74.295 MHz) of the Fabry-Perot. The spacing of the transmission peaks does not always agree with the grid spacing. To construct an improved frequency scale, nearly linear in dye laser frequency rather than proportional to the analog voltage, we use the Fabry-Perot peaks as equidistant frequency markers. To determine their position as well as possible, we fit the transmission Airy formula, which is the theoretical description of the transmitted intensity,²⁴ to each pair of neighboring peaks. This gives us the change in dye laser voltage corresponding to the free spectral range of the Fabry-Perot, for each pair of neighboring peaks. A new frequency scale is then constructed by linear interpolation between the peaks. Figure 5(b) shows the spectrum of Fig. 5(a) plotted against the new linearized frequency scale; the improvement is obvious. We have further checked this procedure by comparing the iodine spectra [Fig. 4(c)] of several different scans over the same frequency range. The linearization of the frequency scale leads to excellent agreement between the respective peak positions of different I₂ scans. The frequency scales of all experimental spectra shown in the following sections have been linearized by this procedure. Furthermore, we can establish a common frequency scale for different scans by overlapping their respective iodine spectra [Fig. 4(c)]. This procedure is legitimate only for spectra taken

on the same day, because the lock point of the Ar⁺ laser will differ from day to day. A common frequency scale for scans from different days may still be established by overlapping non-Stark-broadened scans taken under identical conditions. Spectra for most experimental conditions have been recorded several (up to 20) times. The spectra actually shown are typical examples of the spectra with good signal-to-noise ratio.

A. Beam profiles

Using the arrangement described in Sec. III we have obtained profiles of the laser beams in cell 2, which will be used to estimate the peak energy density and intensity in cell 1. To obtain transverse beam profiles we scan a 5- μ m slit across the respective laser beam which has been reflected out of cell two with the help of an optional beam splitter, as shown in Fig. 3. Such profiles are shown, as solid lines, for the cw Ar⁺ and the pulsed dye laser beam in Fig. 6(a) and Fig. 6(b), respectively. To determine the beam radius $(1/e^2$ points of the intensity), we have fitted



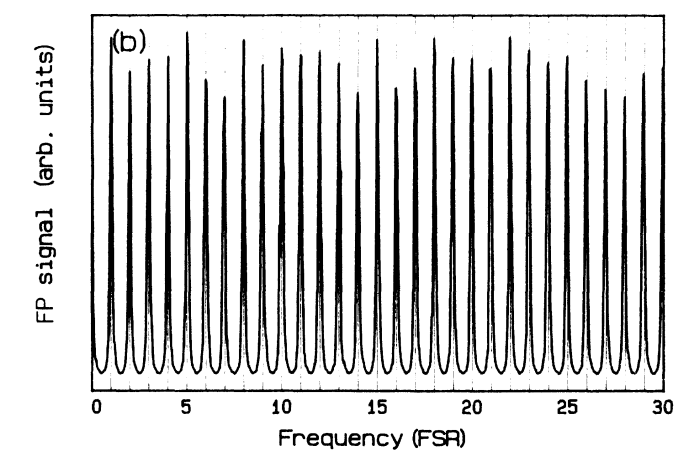


FIG. 5. Part of the Fabry-Perot spectrum in Fig. 4(d). (a) Frequency scale derived from dye laser scan voltage. (b) Linearized frequency scale derived from Fabry-Perot peaks.

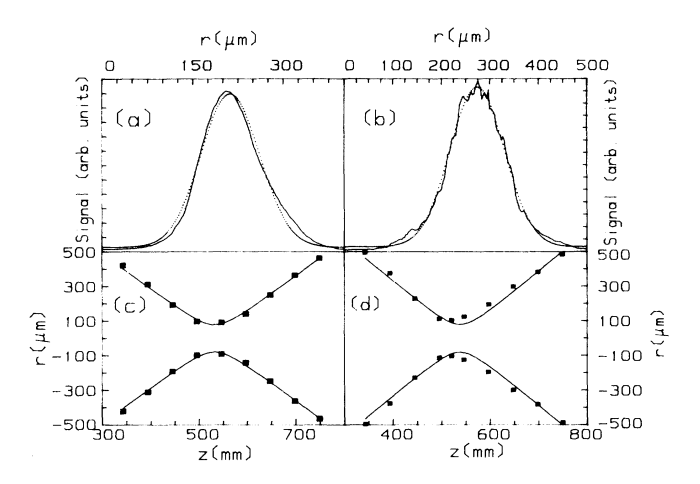


FIG. 6. Results of beam profiling. (a) Beam profile of the cw Ar⁺ laser (solid line) together with a Gaussian fit (dotted line). (b) Beam profile of the pulsed dye laser (solid line) together with a Gaussian fit (dotted line). (c) Measured beam radii of the cw Ar⁺ laser (squares) together with a theoretical fit (solid curves). (d) Measured beam radii of the pulsed dye laser (squares) together with a theoretical fit (solid curves).

Gaussian functions (dotted lines) to both curves. We note that, despite a slight asymmetry, the experimental results agree rather well with the Gaussian fit. Nine to ten transverse beam profiles were acquired for each beam, varying the distance from the focusing lens by roughly 5 cm (2") between the individual profiles. The resulting beam radii (squares) together with a theoretical fit (solid line), which describes the beam sizes along the propagation axis, are shown in Figs. 6(c) and 6(d). The theoretical fit assumes that the Rayleigh length z_0 and the spot radius w_0 are related by $z_0 = \pi w_0^2 / \lambda$, where λ is the laser wavelength. We note that while we do not have perfect Gaussian beams, the Gaussian approximation with identical parameters for both beams appears to be reasonable. According to Fig. 6(d), the focus of the pulsed beam occurs in a distance of $z_2 = 540 \text{ mm} \pm 5\%$ from the imaging lens with a spot radius of $w_{02} = 80 \,\mu\text{m} \pm 20\%$. The error limits are not the result of a statistical analysis of the fit, but an educated guess. We use geometrical optics to calculate the spot radius in cell one as

$$w_{01} = w_{02} \frac{f}{z_2 - f} = 8.2 \ \mu \text{m} \pm 21\%$$
 (17)

The measured average power of the pulsed dye laser is 55 mW $\pm 20\%$ at a repetition rate of 10 Hz, corresponding to an energy of 5.5 mJ $\pm 20\%$ per pulse. We use a standard formula for Gaussian beams to calculate the peak energy density at the focal point (z=0, r=0) as

$$E_0^{\text{den}} = \frac{2}{\pi} \frac{E}{w_0^2} = 5.2 \times 10^7 \frac{J}{\text{m}^2} \pm 45\%$$
 (18)

To estimate the peak intensity of the dye laser pulse, we have measured its time evolution with a fast photodiode (rise time < 100 psec) and a 500 MHz storage oscilloscope. While the time evolution shows some irregular

spiking due to the beating of longitudinal modes in the Nd-YAG laser cavity, we have chosen to model the time evolution with a Gaussian function as

$$I(t) = I_0 \exp\left[-\frac{\ln(2)}{\delta t^2} t^2\right], \qquad (19)$$

where δt stands for the measured half-width at half maximum (HWHM) of $\delta t = 3$ nsec $\pm 30\%$. Integrating over this time evolution we relate the peak intensity in space and time I_0 to the maximum spatial energy density $E_0^{\rm den}$

$$I_0 = \left[\frac{\ln(2)}{\pi}\right]^{0.5} \frac{E_0^{\text{den}}}{\delta t} = 8 \times 10^{15} \text{ W/m}^2 \pm 55\%$$
, (20a)

or directly to the measured parameters

$$I_0 = \frac{2}{\pi} \left[\frac{\ln(2)}{\pi} \right]^{0.5} \frac{E}{\delta t} \left[\frac{z_2 - f}{w_{02} f} \right]^2 = 8 \text{ GW/mm}^2 \pm 55\% .$$
(20b)

Due to the large accumulative error of this measurement, we will use the value for the peak intensity only as an order-of-magnitude estimate.

B. Stark broadened SRS spectra

To calculate Stark-broadened SRS spectra we use equations which describe the SRS signal generation in focused Gaussian beams.⁷ The total power of the IRS signal as used in our experiment is

$$\Delta P_2 = -\frac{16}{\pi w_0^4} \frac{k_2}{c \epsilon_0} P_1 P_2 \int_{z_1}^{z_2} dz \int_0^{\infty} dr \, r \chi''(P_1, r, z) G_I^2 ,$$
(21a)

where G_I is the Gaussian intensity distribution

$$G_I(r,z) = I_0 \left[1 + \left(\frac{z}{z_0} \right)^2 \right]^{-1} \exp \left[\frac{-2(r/w_0)^2}{1 + (z/z_0)^2} \right],$$
 (21b)

 P_1 and P_2 are, respectively, the incident pump- and probe-laser powers, which may be a function of time, and ΔP_2 is the change in probe power, i.e., the IRS signal.

Due to the Stark effect, χ'' , the imaginary part of the third-order nonlinear susceptibility $\chi^{(3)}$ is a function of laser power and spatial position. Since the pump-laser intensity is in our case far higher than the probe-laser intensity, it is the sole cause of the Stark effect. We have to adapt Eqs. (21) to our experiment which uses parallel polarized lasers and a detection system which is not polarization sensitive, χ'' stands therefore for the tensor element χ''_{3333} . A pulsed pump laser and a cw probe laser result in a pulsed signal, which is integrated by the detection system over the duration of each pulse, yielding the SRS energy per pulse. Therefore we have to include an integration over the time evolution of the pulsed laser into our theoretical results. The length of the interaction region in cell one (≈ 10 cm) is about 200 times larger than the Rayleigh length ($z_0 \approx 0.36$ mm); the limits of integration z_1 , and z_2 can therefore be approximated by $-\infty$ and $+\infty$, respectively. Taking all of the above into account and neglecting proportionality constants, which do not influence the line shape, we may rewrite Eq. (21) as

$$\Delta E \sim \int_{-\infty}^{\infty} dt \ e^{-at^2} \int_{-\infty}^{\infty} dz \int_{0}^{\infty} dr \ \chi^{\prime\prime} G_I^2 \ , \tag{22}$$

where ΔE is the energy of the SRS signal generated by one laser pulse, e^{-at^2} is the Gaussian approximation of the time evolution of the dye laser intensity, with

 $a = \ln(2)/\delta t^2$ and $\delta t = 3$ nsec being the HWHM. Due to the Stark effect χ'' is a function of the Stark coefficient β and the local pump intensity, which is a function of t, z, and r. Under our experimental conditions we may neglect phase modulation induced by the rapid Stark tuning of the molecular transition frequency²⁵ and include the Stark shift directly in the Lorentzian part of χ'' . For a Q-branch vibrational-rotational transition $(v=0 \rightarrow v=1) \chi''$ may be written as [Eq. (8a)]

$$\chi_L''(\Delta\omega) = B \sum_{l=0,\infty} \sum_{m=-l,l} F_{1,l,m}^{0,l,m} \frac{\gamma}{\left[\Delta\omega + \beta_{1,l,m}^{0,l,m} I(t,z,r)\right]^2 + \gamma^2} , \qquad (23a)$$

where B is a constant, $\Delta\omega$ has been defined as $\Delta\omega = \Delta - \omega = \Delta - (\omega_2 - \omega_1)$, and the pump intensity I, which induces the Stark shift βI , may be written as

$$I(t,z,r) = I_0 e^{-at^2} G_I(z,r)$$
 (23b)

To obtain χ'' including Doppler broadening and laser linewidth, we convolute χ''_L with the respective Doppler and laser line shapes³ G and P as

$$\chi'' = \chi_L'' * G * P . \tag{23c}$$

We have used Eqs. (23) to calculate Stark-broadened SRS line shapes for the l=4 vibrational-rotational transition in the Q branch of N_2 for various peak intensities I_0 . The summation over l in Eq. (23a) has proven to be unnecessary in these SRS calculations, since compared to the Stark broadening the influence of neighboring lines turned out to be negligible. Results, with the maximum signal normalized to 1, are shown in Fig. 7 for peak intensities between 0 and 16 GW/mm². We note that at a fairly low peak intensity ($I_0=1$ GW/mm²) the spectral peak is shifted and the line shape somewhat broadened towards higher frequency (smaller Raman shift). At higher intensities the peak shift increases only minimally, while the asymmetric broadening significantly changes

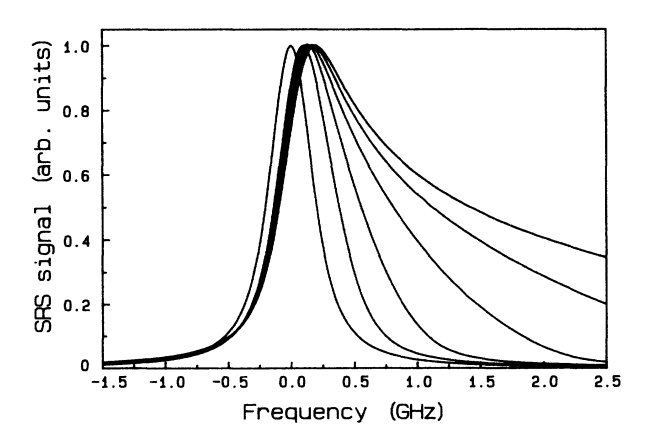


FIG. 7. Theoretical SRS spectra of the l=4 vibrational Q-branch transition ($v=0 \rightarrow v=1$) in molecular nitrogen for peak intensities of $I_0=0,1,2,4,8,16$ GW/mm², as a function of $\Delta\omega$.

the line shape and linewidth. A qualitative explanation of this result may be found in the fact that at high intensities, the signal generated close to the origin (t,z,r=0) is spread in frequency due to the large range of Stark shifts. The spectral peak is, however, still due to the nearly unshifted signal, generated away from the origin in time and space (r,z,t=0) at fairly small intensities. This leads to small peak shifts together with a strong asymmetric broadening of the wings.

An experimental IRS spectrum of the l=4 vibrational Q-branch transition in nitrogen, which shows substantial Stark broadening, together with a theoretical calculation is shown in Fig. 8(a). To overlay theoretical and experimental curves, we have fitted only peak intensity and zero offset of the signal. This fitting procedure has led to a peak intensity of 4.8 GW/mm², within the limits given by our beam profiling results (8 GW/mm²⁺ \pm 55%). The common frequency scale for theory and experiment has not been adjusted; it is simply that of the non-Starkbroadened spectrum from a subsequent measurement. We have chosen the peak of the theoretical fit to this non-Stark-broadened spectrum as the zero of our frequency scales³ for l=4. As described in the beginning of Sec. III, we use the respective Fabry-Perot spectra to define relative linear frequency scales for both spectra. Then we overlay the multitude of iodine hyperfine lines [Fig. 4(c)] of one scan with those of the other scan. This way we transfer the zero of the frequency scale from the non-Stark-broadened to the Stark-broadened spectrum. A comparison with the theory therefore evaluates not only the prediction of the line shape for the Starkbroadened spectra, but also the prediction of the shift between non-Stark-broadened and Stark-broadened SRS spectra. Figure 8(a) shows good agreement between theory and experiment. Minor disagreements in the line shape are probably due to the imperfect assumption of identical Gaussian profiles for pump and probe laser and the rather crude approximation of a Gaussian time evolution of the pump-laser intensity. Figure 8(b) shows the experimental result together with calculated spectra corresponding to peak intensities of 4.0, 4.8, and 5.5 GW/mm². We note that a change of about 15% in peak intensity corresponds to a noticeable change in line

To directly compare non-Stark-broadened and Stark-broadened IRS spectra of l=4 we have applied a 25-point

smoothing routine²⁶ to subsequently taken non-Stark-broadened and Stark-broadened spectra. The resulting experimental IRS spectra are both shown in Fig. 8(c). One recognizes directly the major influence of the Stark effect on line shape and peak position. The Stark-broadened IRS spectrum was taken with cell 1 filled with 10 kPa of nitrogen and cell 2 evacuated, while we have reversed this situation to record the non-Stark-broadened IRS spectrum. Due to the fact that we have left all other experimental parameter unchanged, Fig. 8(c) represents a rather direct comparison between Stark-broadened and non-Stark-broadened IRS spectra. Figure 8(d) shows the same comparison for the theoretically calculated SRS

spectra. The similarity between Figs. 8(c) and 8(d) is evident.

The same analysis was performed for scans of the l=12 vibrational Q-branch transition in molecular nitrogen, resulting in equally good agreement between theory and experiment.¹¹

C. Stark-broadened FWMRS spectra

To calculate Stark-broadened FWMRS spectra we follow similar procedures as for SRS. The generation of CSRS signal in focused Gaussian beams is described by⁷

$$P_{3} = \frac{2k_{3}^{2}k^{2}}{\pi^{2}c^{2}\epsilon_{0}^{2}}P_{1}^{2}P_{2}\int_{0}^{\infty}dx\left|\int_{z_{1}}^{z_{2}}dz\,e^{ixz/4}\frac{e^{-i\tan^{-1}z}}{(1+z^{2})^{3/2}}\int_{0}^{\infty}dr\,r\chi^{(3)*}J_{0}(x^{1/2}r)\exp\left[r^{2}\left[\frac{iz-3}{1+z^{2}}\right]\right]\right|^{2},$$
(24)

where J_0 is the zero-order Bessel function, x is a dummy variable, and r and z are written in units of spot radius w_0 and Rayleigh length z_0 , respectively. Equation (24) is adapted to the experimental situation by making the pump-laser in-

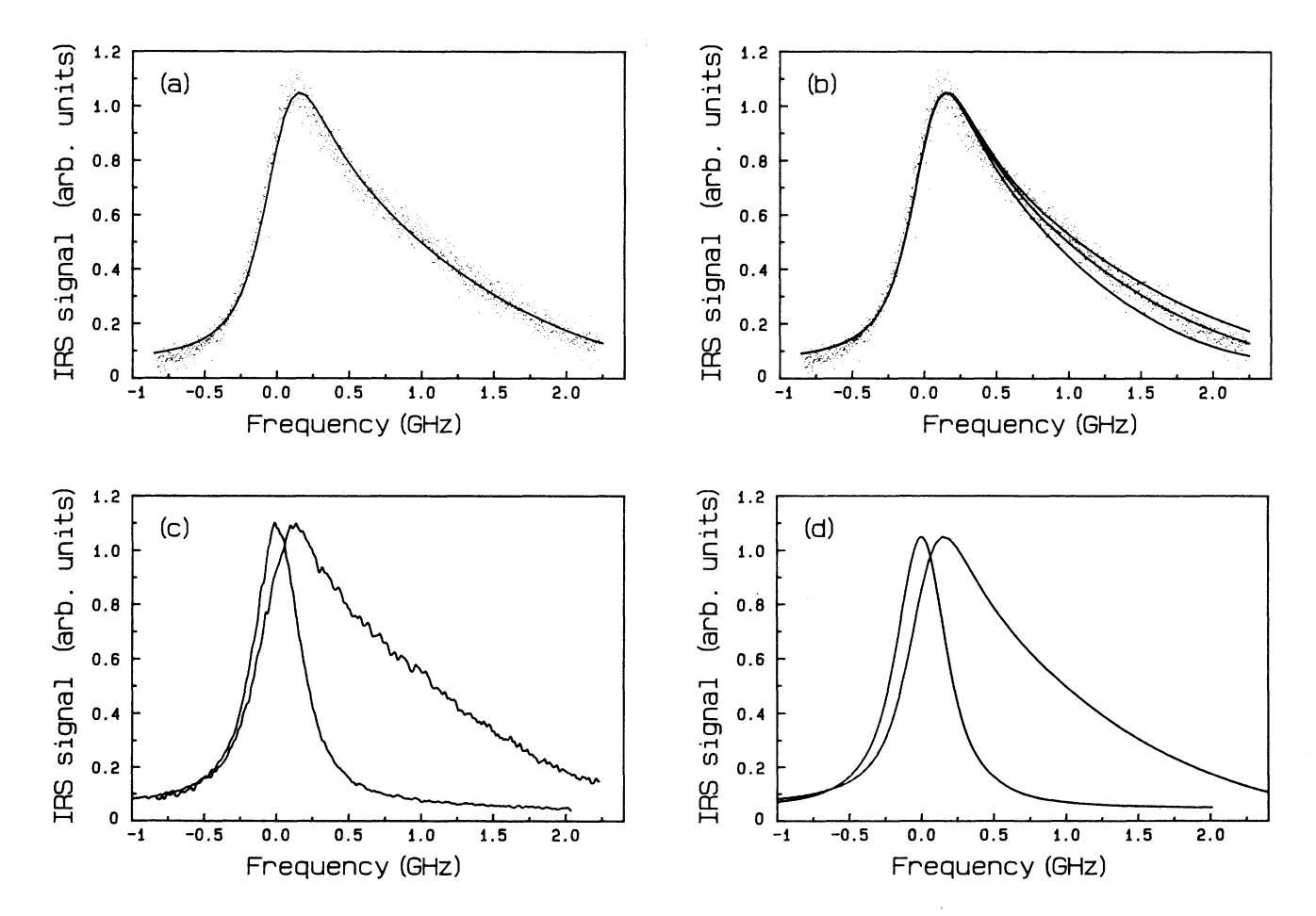


FIG. 8. Stark broadened Raman spectra of the l=4 vibrational Q-branch transition ($v=0 \rightarrow v=1$) in molecular nitrogen as a function of $\Delta\omega$; i.e., with the dye laser scanned towards higher frequency (smaller Raman shift). (a) Comparison between theoretical (solid curve, $I_0=4.8~{\rm GW/mm^2}$) and experimental (dots) IRS spectra. (b) Comparison between theoretical (solid line, $I_0=4.0$, 4.8, and 5.5 GW/mm²) and experimental (dots) IRS spectra. (c) Comparison between non-Stark-broadened and Stark-broadened experimental IRS spectra. (d) Comparison between non-Stark-broadened ($I_0=4.8~{\rm GW/mm^2}$) theoretical IRS spectra.

tensity a Gaussian function of time, corresponding to a pulsed pump laser. Furthermore, we integrate the whole expression over time, which corresponds to a detection scheme which is non-time resolved for any laser pulse, detecting the total emitted energy per pulse. Neglecting all constants which do not influence the line shape we rewrite Eq. (24) for detected energy per pulse as

$$E \sim \int_{-\infty}^{+\infty} dt \ e^{-2at^2} \int_{0}^{\infty} dx \left| \int_{-\infty}^{+\infty} dz \ e^{ixz/4} \frac{e^{-i\tan^{-1}z}}{(1+z^2)^{3/2}} \int_{0}^{\infty} dr \ r \chi J_0(x^{1/2}r) \exp \left[r^2 \left[\frac{iz-3}{1+z^2} \right] \right] \right|^2, \tag{25a}$$

where e^{-at^2} is the Gaussian approximation of the time evolution of the dye laser intensity, with $a = \ln(2)/\delta t^2$ and $\delta t = 3$ nsec being the HWHM. Taking advantage of symmetries in z and t, we rewrite Eq. (25a) as

$$E(\Delta\omega) \sim \int_0^\infty dt \ e^{-2at^2} P(\Delta\omega, I) = \int_0^\infty dt \ e^{-2at^2} \int_0^\infty dx \left| \int_0^\infty dz \int_0^\infty dr \ \chi(\Delta\omega, I) f(r, z, x) \right|^2, \tag{25b}$$

with

$$f(r,z,x) = \exp\left[\frac{-3r^2}{1+z^2}\right] \frac{rJ_0(x^{1/2}r)}{(1+z^2)^2}$$

$$\times \left[\cos\left[\frac{xz}{4} + \frac{zr^2}{1+z^2}\right] + z\sin\left[\frac{xz}{4} + \frac{zr^2}{1+z^2}\right]\right].$$
(25c)

The numerical evaluation of this formula is fairly involved and its basic principles will be described in the following. We note that the integrand in Eq. (25b) consists of two factors. A real function f(r,z,x) of the coordinates r,z and of the dummy variable for integration x, and the complex third-order nonlinear susceptibility $\chi(\Delta\omega,I)$, a function of detuning $\Delta\omega$ and local intensity I(r,z,t), which can be calculated from Eqs. (23) by replacing the imaginary part of the Lorentzian with the complete complex Lorentzian. We change the variable of integration from t to $I_t = I_0 e^{-at^2}$ and obtain

$$E(\Delta\omega, I_0) \sim \int_0^{I_0} dI_t \frac{I_t}{[-a \ln(I_t/I_0)]^{0.5}} P(\Delta\omega, I_t)$$
, (26a)

with

$$P(\Delta\omega, I_t) = \int_0^X dx \left| \int_0^Z dz \int_0^R dr \, f(r, z, x) \chi(I_t, \Delta\omega) \right|^2,$$
(26b)

where X, R, and Z are the upper limits for the numerical integration. A priori it is unclear how to choose these limits and the number of evaluation points in each dimension. We have solved this problem rather pragmatically by increasing the limits and the number of evaluation points until the calculated spectra converge to their final form. This has led to X=20, Z=20, R=10, and 50 evaluation points in each dimension. For these values we estimate the remaining error for any $\Delta \omega$ to be less than 1% of the maximum signal. First, we evaluate the generated power $P(\Delta \omega, I_t)$ on an equidistant two-dimensional grid for different detunings $\Delta \omega$ (72 points, 50-MHz spacing) and intensities I_t (51 points, 0.1 GW/mm² spacing). The

rather complicated function f(r,z,x) is independent of $\Delta \omega$ and I_t and does not have to be reevaluated for different positions on the grid. One part of f(r,z,x) is a Bessel function J_0 , which is calculated by an approximation with rational functions or polynomials, depending on the size of its argument.²⁷ The third-order nonlinear susceptibility $\chi(\Delta\omega, I=0)$, including the appropriate pressure, Doppler, and laser broadening [Eqs. (23)], is first stored in a one-dimensional look-up table. Then we use the complex form of Eq. (23a) to calculate a twodimensional array of χ for 3672 different combinations of $\Delta \omega$ and I, values between these points will be evaluated by linear interpolation. The summation over the rotational quantum number l [Eq. (23a)] is terminated at l=8for the calculation of the spectrum for l=4, this includes all neighboring resonances within ± 30 GHz which can influence the l=4 FWMRS line.³ Finally we use a closed Newton-Cotes formula, the extended trapezoidal rule,²⁷ for the three-dimensional integration, Eq. (26b), calculating 3672 values of $P(\Delta\omega, I_t)$ for the different combinations of $\Delta \omega$ and I_t . Using Microsoft Fortran V4.01 on a 16-MHz Intel 80386 based personal computer with a 80387 numerical coprocessor, this calculation takes

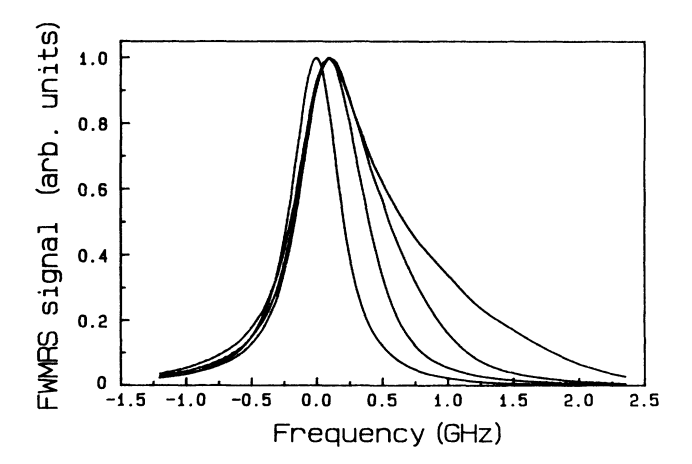


FIG. 9. Theoretical FWMRS spectra of the l=4 vibrational Q-branch transition $(v=0\rightarrow v=1)$ in molecular nitrogen for peak intensities of $I_0=0,1,2,4$ GW/mm², as a function of $\Delta\omega$.

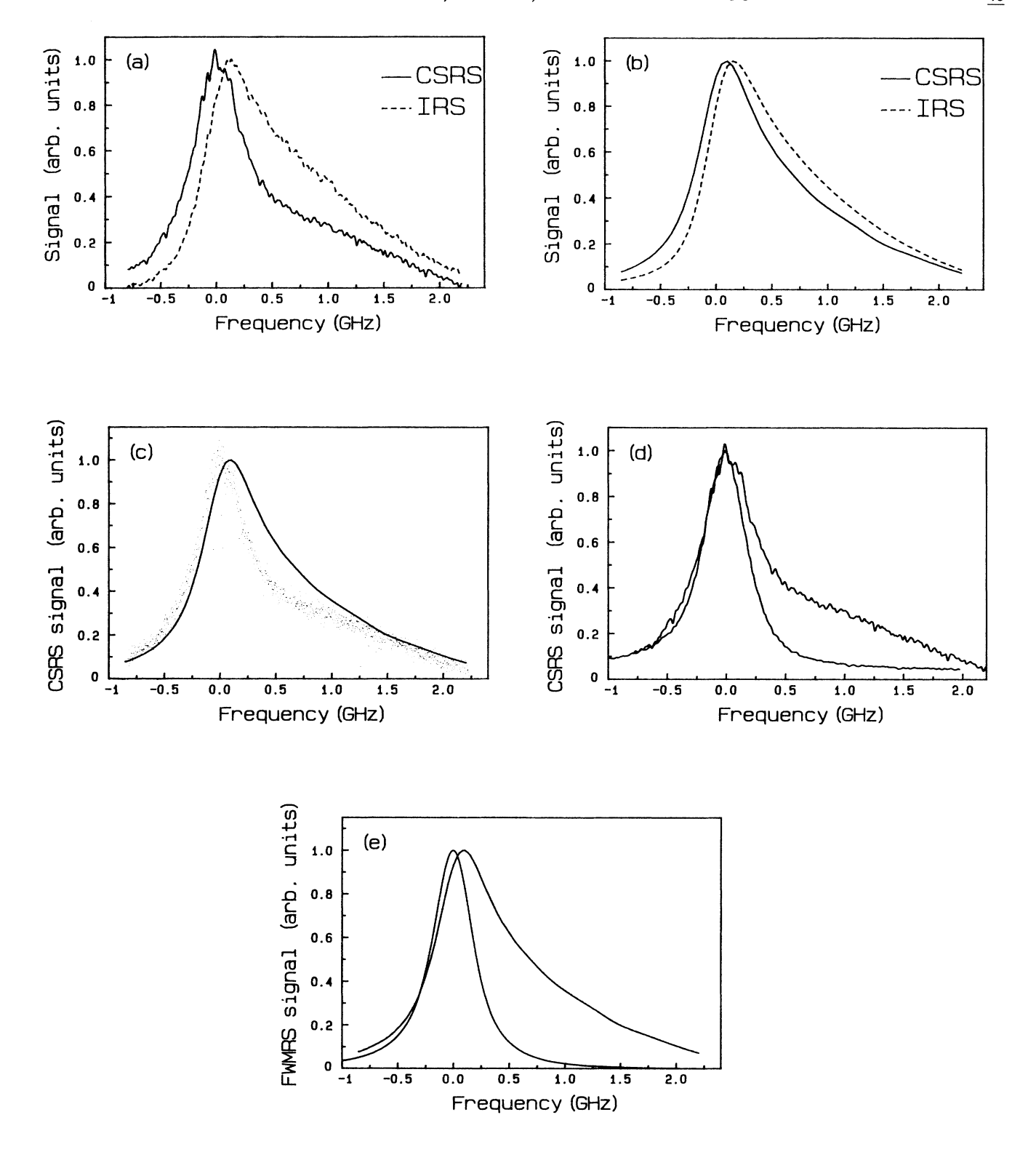


FIG. 10. Stark broadened CRS spectra of the l=4 vibrational Q-branch transition ($v=0 \rightarrow v=1$) in molecular nitrogen as a function of $\Delta \omega$; i.e., with the dye laser scanned towards higher frequency (smaller Raman shift). (a) Comparison between experimental Stark broadened CSRS (solid curve) and SRS (dashed curve) spectra. (b) Comparison between theoretical Stark broadened CSRS (solid curve) and SRS (dashed curve) spectra for $I_0=4.8$ GW/mm². (c) Comparison between theoretical (solid curve, $I_0=4.8$ GW/mm²) and experimental (dots) CSRS spectra. (d) Comparison between non-Stark-broadened and Stark-broadened experimental CSRS spectra. (e) Comparison between non-Stark-broadened ($I_0=4.8$ GW/mm²) theoretical CSRS spectra.

roughly 10 h of computer time, i.e., about 10 s per three-dimensional integration. Now we may calculate the final spectra rather easily via Eq. (36a). To avoid the weak singularity at $I_t = 0$, we use the extended midpoint rule, which is based on the second Euler-Mclaurin summation formula,²⁷ for the final integration.

Results, with the maximum FWMRS signal normalized to 1, are shown in Fig. 9 for peak intensities between 0 and 4 GW/mm². We note that the main peak shift takes place at a relatively low peak intensity $(I_0 < 1)$ GW/mm²). For higher peak intensities I_0 the line shape becomes more asymmetric, but no further shift of the spectral peak is observed. Figure 10(a) shows a comparison between simultaneously recorded Stark-broadened CSRS and IRS spectra of the l=4 vibrational Q-branch transition in nitrogen (25-point smoothing). We note that the peak of the CSRS spectrum is narrower and shows less Stark shift than the peak of the IRS spectrum. Furthermore, the line shape of the CSRS spectrum shows a characteristic kink around $\Delta\omega = 0.3$ GHz. These characteristic features have been repetitively observed in many (\approx 20) individual spectra taken on several different days. The IRS spectrum has previously been successfully fitted with a theoretical spectrum corresponding to a peak intensity of $I_0 = 4.8 \text{ GW/mm}^2$ (Sec. IV B). We compare this theoretical calculation with a calculation of the CSRS spectrum for the same peak intensity [Fig. 10(b)]. It shows less Stark shift and is somewhat narrower than the theoretical IRS spectrum. The CSRS theory reproduces some of the experimental features, it, however, does not reproduce the characteristic CSRS line shape as seen in Fig. 10(a). A direct comparison between the experimental (dots) and the theoretical (solid line) CSRS spectrum is shown in Fig. 10(c). As for IRS (Sec. IV B), peak height and zero offset are adjusted, while the common frequency scale has been experimentally determined. The experimental peak is narrower and shows less Stark shift than the theoretical peak. Furthermore, the theory does not reproduce the characteristic kink mentioned earlier. Figure 10(d) compares a Stark-broadened with a non-Stark-broadened CSRS spectrum. We see, in comparison with the same figure for SRS [Fig. 8(c)], rather little peak shift, a small broadening of the main peak and the characteristic asymmetric wing with a definite kink on the high-frequency side. The theoretical comparison with Stark broadening [Fig. 10(e), $I_0 = 4.8 \, \text{GW/mm}^2$] clearly does not reproduce these experimental findings.

While the reasons for the discrepancies between theoretical and experimental FWMRS spectra are not entirely clear, we will discuss two likely possibilities. The theoretical analysis assumes Gaussian laser beams, with an additional Gaussian time evolution for the pump-laser intensity. In practice the pulsed pump-laser beam deviates from this ideal situation. Whereas the SRS signal varies linearly with the pump laser intensities, the FWMRS signal is proportional to the square of the pump-laser intensity; FWMRS spectra are therefore influenced more strongly by deviations from the ideal Gaussian beam and the spiking in time evolution than SRS spectra. In addition, the contribution of higher-order susceptibilities, such as $\chi^{(5)}$, may alter FWMRS spectra; this will be analyzed in Sec. V.

V. CONTRIBUTIONS OF $\chi^{(5)}$ TO THE FWMRS SIGNAL

The strong electric fields under tight-focusing conditions make it necessary to examine possible contributions of higher-order processes to the FWMRS signal. The susceptibility χ may be expanded in terms of the electrical field as

$$\gamma = \gamma^{(1)} + \gamma^{(2)}E + \gamma^{(3)}E^2 + \gamma^{(4)}E^3 + \gamma^{(5)}E^4 + \cdots$$
 (27)

where all even χ terms are zero for a medium with inversion symmetry, such as a gas. While $\chi^{(3)}$ is the lowest-order contributor to the FWMRS signal, higher-order contributions have to be accounted for under sufficiently high electric fields. In this section we estimate the contribution of the fifth-order susceptibility $\chi^{(5)}$.

The general theoretical expression for $\chi^{(3)}(\omega_1,\omega_2,\omega_3)$ may be written as²⁸

$$\chi_{ijkl}^{(3)} = \frac{1}{4\pi\epsilon_0} \frac{N}{3!h^3} \sum_{a,b,c,d} \frac{R_{ab}^i R_{bc}^i R_{cd}^k R_{da}^l}{(\omega_{ba} - \omega_1 - \omega_2 - \omega_3)(\omega_{ca} - \omega_2 - \omega_3)(\omega_{da} - \omega_3)} , \qquad (28)$$

where the R's are the electric dipole matrix elements between the levels a, b, c, and d, the ω 's are the respective frequencies, and the damping constants have been neglected. This expression can be pictured as a sum over 24 non-time-ordered single-sided Feynman diagrams, or more correctly a sum over 48 time-ordered double-sided Feynman diagrams.²⁹ In the case of two-beam FWMRS, a and c are the levels of the Raman transition, $\omega_1 = \omega_3 > 0$, $\omega_2 < 0$, and the second term in the denominator determines the Raman resonance. In this case only the four double-sided diagrams shown in Fig. 11 result in a Raman resonance and contribute significantly to the FWMRS signal. Using the rather crude approximations

$$R = R_{ab}^{i} = R_{bc}^{j} = R_{cd}^{k} = R_{da}^{l} , \qquad (29a)$$

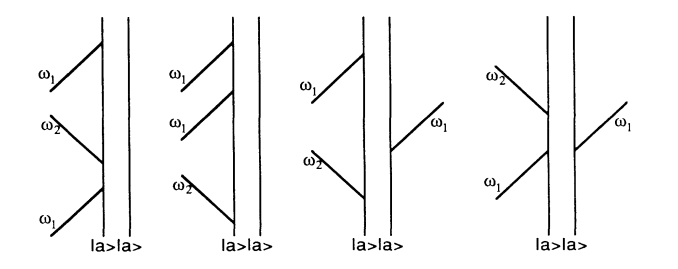


FIG. 11. Double-sided time-ordered Feynman diagrams of third-order nonlinear processes which contribute to the FWMRS signal.

$$\omega_{nr} = \omega_{ba} - \omega_1 - \omega_2 - \omega_3 = \omega_{da} - \omega_3 , \qquad (29b)$$

and the identity

$$\omega_r = \omega_{ca} - \omega_2 - \omega_3 , \qquad (29c)$$

we may write Eq. (34) for FWMRS as

$$\chi_{ijkl}^{(3)} = \frac{4}{4\pi\epsilon_0} \frac{N}{3!h^3} \frac{R^4}{\omega_r \omega_{nr}^2} , \qquad (29d)$$

where the factor of 4 comes from the summation over the four diagrams. Comparing this expression with Eq. (8a), which expresses $\chi^{(3)}$ approximately as $\widetilde{A}_{1}^{0}(a_{1}^{0})^{2}$, we can calculate $R^{2}/(h\omega_{nr})$ for the $v=0 \rightarrow v=1$ vibrational Q branch in N_{2} for no Stark effect, using the values of a_{1}^{0} given in Table I and identifying ω_{r} with $\Delta\omega-i\gamma$, as

$$\frac{R^2}{h\omega_{\rm nr}} = 3^{1/2}\pi\epsilon_0 a_1^0 = 3.3 \times 10^{-41} \frac{C^2 m^2}{J} . \tag{30}$$

Similar to $\chi^{(3)}$, we can express $\chi^{(5)}$ in double-sided Feynman diagrams. Only four of them (Fig. 12), which correspond on a one-to-one basis to the $\chi^{(3)}$ diagrams in Fig. 11, result in $\chi^{(5)}$ terms with an additional resonance denominator and contribute significantly to FWMRS. Essentially we have added a Rayleigh interaction to the upper Raman level c, as can be seen from a comparison of Fig. 11 with Fig. 12. Using the approximations of Eqs. (29) we write the part of $\chi^{(5)}$ which contributes to the FWMRS signal as

$$\chi_{ijkl}^{(5)} = \frac{4}{4\pi\epsilon_0} \frac{N}{5!h^5} \frac{R^6}{\omega_r^2 \omega_{nr}^3} . \tag{31}$$

With the help of Eq. (27) the nonlinear susceptibility relevant to FWMRS becomes

$$\chi = E^2 \chi^{(3)} \left[1 + \frac{|E|^2}{20h\omega_r} \frac{R^2}{h\omega_{nr}} \right] \sim I \chi^{(3)} \left[1 + A \frac{I}{\omega_r} \right],$$
(32a)

with

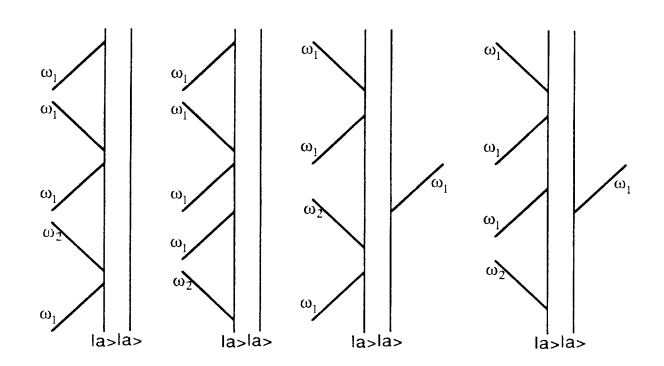


FIG. 12. Double-sided time-ordered Feynman diagrams of fifth-order nonlinear processes which contribute to the FWMRS signal.

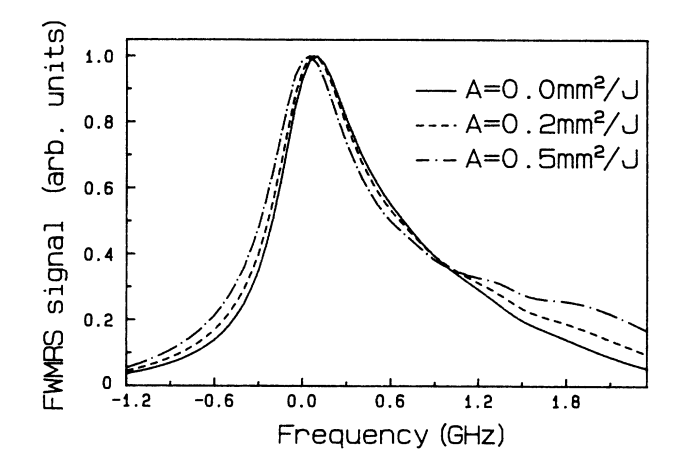


FIG. 13. Theoretical FWMRS spectra of the l=4 vibrational Q-branch transition ($v=0 \rightarrow v=1$) in molecular nitrogen for fifth-order coefficients of A=0.0,0.2,0.5 mm²/J and a peak intensity of 4.8 GW/mm², as a function of $\Delta\omega$.

$$A = \frac{1}{10c\epsilon_0 h} \frac{R^2}{h\omega_{nr}}$$
= 1.9 × 10⁻⁶ $\frac{\text{m}^2}{\text{J}}$ = 1.9 $\frac{\text{mm}^2}{\text{J}}$ = 1.9 GHz mm²/GW
(32b)

for the vibrational Q branch of molecular nitrogen. Due to the crudeness of our approximations this value is only expected to give sign and order of magnitude of the constant A.

We use Eq. (32a), with A treated as an adjustable parameter, to examine the influence of the fifth-order process on the Stark-broadened FWMRS line shapes analyzed in Sec. IV C. Inserting the new expression for $\chi(\Delta\omega,I)$ [Eq. (32a)] into Eq. (25) enables us to calculate

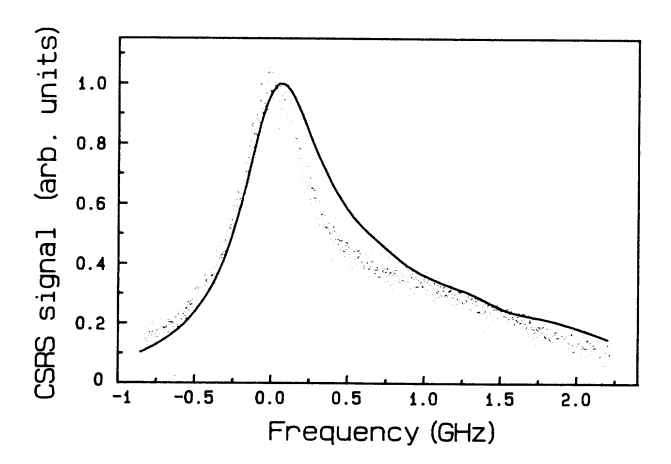


FIG. 14. Comparison between experimental (dots) and theoretical (solid curve, $I_0=4.8~{\rm GW/mm^2}$, fifth-order coefficient $A=0.3~{\rm mm^2/J}$) CSRS spectra of the l=4 vibrational Q branch in N_2 .

theoretical FWMRS spectra for different values of A. Figure 13 shows FWMRS spectra for l=4, a peak intensity I_0 of 4.8 GW/mm² and fifth-order coefficients A of 0.0, 0.2, and 0.5 mm²/J. Increasing the coefficient A shifts the spectral peak to a lower frequency $\Delta \omega$ and raises the high-frequency wing.

Adjusting the parameter A to achieve a good fit with the experimental spectrum plotted in Fig. 10(c) (l=4, I_0 =4.8 GW/mm²) leads to A=0.3 mm²/J and to significantly improved agreement between experiment and theory (Fig. 14), due to the additional $\chi^{(5)}$ term. This fitted A value is well within one order of magnitude of the theoretical estimation, which is an appropriate agreement.

While our experiment has not been designed to test the possible influence of higher-order effects, its results nevertheless suggest that the fifth-order process leading to a fifth-order nonlinear susceptibility $\chi^{(5)}$ may be important and should perhaps be included in the line-shape theory for tightly focused high-power laser beams. It will be necessary however, to investigate this possibility along with the possible inclusion of even higher-order effects with a specifically designed experiment.

VI. CONCLUSIONS

With our theoretical and experimental investigations, we have made progress in the understanding of coherent Raman spectroscopy (CRS) line shapes for high laser intensities in the interaction region. The line shapes of the two most important CRS's, stimulated Raman spectroscopy (SRS) and four-wave mixing Raman spectroscopy (FWMRS), have been compared in detail, using a novel experimental setup capable of utilizing both spectroscopic techniques simultaneously.

We have studied the influence of optical Stark effect, due to the high pump laser intensity in focused Gaussian beams, on both types of CRS's. For the theoretical calculation of Stark-broadened spectra, we have used a new theory of FWMRS signal generation in Gaussian beams.⁷ This theory and the respective theory for SRS, which is

well known, have then been combined with our calculation of Stark coefficients and transition strengths for the individual orientational sublevels in N_2 , to yield theoretical stark-broadened line shapes for both SRS and FWMRS.

Experimentally we have rapidly alternated between the simultaneous measurement of SRS and FWMRS spectra at low (mild focusing) and high (tight focusing) pump laser intensities. This alternation together with a sophisticated frequency reference scheme has enabled us to make a rather direct comparison between Starkbroadened and non-Stark-broadened spectra.

The experimental results show a very small peak shift for FWMRS and a larger peak shift in the order of 10% of the maximum Stark shift, βI_0 , for SRS. The wings of the Raman lines are very asymmetrically broadened in the direction of the theoretical Stark shift for both CRS's. This asymmetric wing is somewhat more pronounced for SRS than for FWMRS, where it shows a characteristic kink. The SRS results are in excellent agreement with our theory, while the FWMRS results show only partial agreement with the theory. We suspect two reasons for the discrepancy. First, FWMRS spectra are more susceptible to deviations of our pump-laser beam from the ideal Gaussian shape in time and space, which has been assumed in the theory. Second, we have analyzed a potential contribution of the fifth-order nonlinear susceptibility $\chi^{(5)}$ to the FWMRS signal and show that its inclusion leads to an improved agreement between experiment and theory. This possibility should motivate further experiments, specifically designed to test the contribution of $\chi^{(5)}$ to FWMRS signals.

ACKNOWLEDGMENTS

The authors are grateful to Dr. R. J. Exton, NASA Langley Research Center, Hampton, for helpful discussions and encouragement. This work was supported in part by the U.S. Department of Defense under University Instrumentation Grant No. DAAL03-86-G-0114.

¹W. M. Tolles, J. W. Nibler, J. R. McDonald, and A. B. Harvey, Appl. Spectrosc. 31, 253 (1977).

²P. Esherick and A. Owyoung, in *Advances in Infrared and Raman Spectroscopy*, edited by R. J. H. Clark and R. E. Hestor (Heyden & Son, London, 1982), Vol. 9.

³H. Moosmüller and C. Y. She, J. Opt. Soc. Am. **B4**, 1977 (1987).

⁴L. A. Rahn, R. L. Farrow, M. L. Koszykowski, and P. L. Mattern, Phys. Rev. Lett. 45, 620 (1980).

⁵R. L. Farrow and L. A. Rahn, Phys. Rev. Lett. **48**, 395 (1982).
⁶L. Li, B. X. Yang, and P. M. Johnson, J. Opt. Soc. Am. **B2**, 748 (1985).

⁷H. Moosmüller, S. B. Anderson, and C. Y. She, preceding paper, Phys. Rev. A 40, 6977 (1989).

⁸A. C. Eckbreth, G. M. Dobbs, J. H. Stufflebeam, and P. A. Tellex, Appl. Opt. 23, 1328 (1984).

⁹E. J. Beiting, Appl. Opt. **25**, 1684 (1986).

¹⁰C. Y. She, H. Moosmüller, and G. C. Herring, Appl. Phys.

B46, 283 (1988).

¹¹H. Moosmüller, Ph.D. dissertation, Colorado State University, 1988.

¹²Y. R. Shen, The Principles of Nonlinear Optics (Wiley, New York, 1984), p. 149.

¹³A. R. Edmonds, Angular Momentum in Quantum Mechanics (Princeton, New Jersey, 1957), p. 21.

¹⁴E. Merzbacher, Quantum Mechanics (Wiley, New York, 1975), p. 186.

¹⁵E. Merzbacher, Quantum Mechanics (Wiley, New York, 1975), p. 396.

¹⁶G. Placzek and E. Teller, Z. Phys. **83**, 209 (1933).

¹⁷Y. R. Shen, The Principles of Nonlinear Optics (Wiley, New York, 1984), p. 28.

¹⁸S. R. Langhoff, C. W. Bauschlicher, Jr., and D. P. Chong, J. Chem. Phys. **78**, 5287 (1983).

¹⁹A. Lofthus and P. H. Krupenie, J. Phys. Chem. Ref. Data 6, 113 (1977).

- ²⁰N. J. Bridge and A. D. Buckingham, Proc. R. Soc. London Ser. A 295, 334 (1966).
- ²¹G. R. Alms, A. K. Burnham, and W. H. Flygare, J. Chem. Phys. 63, 3321 (1975).
- ²²P. Drell and S. Chu, Opt. Commun. 28, 343 (1979).
- ²³L. Hlousek, S. A. Lee, and W. M. Fairbank, Jr., Phys. Rev. Lett. **50**, 328 (1983).
- ²⁴W. Demtröder, Laser Spectroscopy (Springer, Heidelberg, 1981), p. 154.
- ²⁵H. Moosmüller, D. A. Krueger, and C. Y. She, Phys. Rev. A

- 38, 6210 (1988).
- ²⁶P. R. Bevington, Data Reduction and Error Analysis for the Physical Sciences (McGraw-Hill, New York, 1969), p. 255.
- ²⁷W. H. Press, B. P. Flannery, S. A. Teukolsky, and W. T. Vetterling, *Numerical Recipes: The Art of Scientific Computing* (Cambridge University Press, Cambridge, 1986).
- ²⁸P. N. Butcher, *Nonlinear Optical Phenomenon* (Ohio State University Press, Columbus, 1965), p. 80.
- ²⁹Y. Prior, IEEE J. Quantum Electron. **QE-20**, 37 (1984).